Identification of Dynamic Green's Functions in Structural Networks

Alfred S. Carasso* and Emil Simiu†
National Bureau of Standards, Gaithersburg, Maryland

This paper presents the mathematical and computational basis of a method for experimentally identifying the dynamic behavior of linear structural systems. The method consists of exciting the structure with specific pulses and reconstructing the dynamic Green's functions by deconvolution of the measured response. The reconstruction procedure involves the solution of an ill-posed integral equation in the presence of noise. Inverse Gaussian functions, which have mathematical properties that render the deconvolution problem tractable, are used as probing pulses. Two examples are presented for which dynamic Green's functions are reconstructed from synthetic response data: 1) a nondispersive medium consisting of a mechanical slider with free body motion, and 2) a network that may be representative of a large orbiting structure with rigidly connected torsional members and Timoshenko beams. It is shown that residual effects of noise that may be detectable in the reconstructed Green's functions are effectively smoothed out when these functions are used to predict the response to forces such as may be induced by control systems. Finally, an example is presented of deconvolution implemented in *slow motion.*

Introduction

IN various applications, it is convenient to characterize the dynamic behavior of a linear time invariant system in terms of its time-domain impulse response or dynamic Green's function.[1] Such applications include the prediction of responses in structural members or networks, and the development of control strategies in large space structures.[2,3]

A variety of techniques can be brought to bear on problems of structural identification, and useful assessments of the state-of-the-art may be found in Refs. 4–6. The approach to be presented here aims at a direct recovery of the system's Green's function by deconvolution of the response to a time-domain pulse approximating the Dirac δ-function. As such, it is motivated by the same considerations of efficiency and wide applicability as is the technique of Ref. 6, and it falls in the same category of structural identification tools.

The method is designed in full recognition of the fact that such reconstruction is an *ill-posed* problem in the presence of noise, and that only weak constraints, in the form of mean square (L^2) norm a priori bounds on the unknown solution and on the noise content in the data, are generally applicable. For this reason, a specific pulse shape is advocated that allows for a useful notion of *partial deconvolution.* Error bounds can be obtained for each partial deconvolution as a function of the noise level in the data, whereas such bounds are impossible for the desired total deconvolution, i.e., the reconstructed impulse response. This is a mathematical consequence of the fact that dynamic Green's functions in wave propagation problems are typically not smooth functions of time, and a priori *smoothness* constraints can, therefore, not be imposed on the unknown solution in any regularization procedure. However, in the present method, at low levels of noise, one can validate the final reconstruction in most cases of practical interest by using the sequence of increasingly sharp partial deconvolutions as a diagnostic tool. We remark that the "log-convex" error bounds [Eq. (5.17) in Ref. 7] for the partial deconvolutions that characterize this method are, in fact, *best possible.* Thus, stronger error bounds are possible only for problems in which stronger constraints can be placed on the unknown solution, and more precise information regarding the noise process is available. As one example, if the power spectra of both the data noise and the unknown solution can be specified in advance, Wiener filtering is an excellent deconvolution technique.

In this paper we shall describe the intuitive basis behind the method and illustrate its potential application in structural identification, using a minimum of mathematical detail. A full mathematical discussion, along with an effective computational algorithm and its application to the reconstruction of elastic Green's functions, is given in Ref. 7. We first discuss a class of pulses for which the deconvolution problem can be approached satisfactorily. We then derive exact Green's functions for two interesting structures, and use these functions to create synthetic data simulating the responses to specified probing pulses. This is accomplished by numerical convolution of the probe pulse with the structure Green's function, followed by superimposition of noise at levels that may be representative of measurement and transmission devices. It is then shown that the proposed deconvolution technique yields highly accurate reconstructions of the complicated Green's functions for the two structures.

The effort presented in this paper is part of an ongoing project conducted at the National Bureau of Standards, which includes the development of a space-rated actuator capable of producing mathematically specified mechanical pulses.

Pulse Probing and Deconvolution

We consider smooth approximations to $\delta(t)$ that can be synthesized, yet have additional mathematical properties that lead to a well-understood deconvolution problem. An example is the 'inverse Gaussian' pulse:

$$p(\sigma,t) = \frac{\sigma U(t)\exp(-\sigma^2/4t)}{\sqrt{4\pi t^3}}, \qquad -\infty < t < \infty \tag{1}$$

In Eq. (1), σ is a preselected fixed positive parameter that controls the rise time and width of the pulse, and $U(t)$ is the

---

Received Jan. 18, 1988; revision received May 13, 1988. This paper is declared a work of the U.S. Government and is not subject to copyright protection in the United States.

*Research Mathematician, Center for Applied Mathematics.

†NBS Fellow, Center for Building Technology.

Heaviside unit step function; in particular, $p(\sigma,t)$ vanishes for $t \leq 0$. For each fixed σ and all t, $p(\sigma,t)$ is an infinitely differentiable function of t. Hence, there are no discontinuities in $p(\sigma,t)$, nor in any of its derivatives at $t = 0$. Moreover, $p(\sigma,t)$ is positive when t is positive, and

$$\int_0^\infty p(\sigma,t)\,\mathrm{d}t = 1 \tag{2}$$

For small $\sigma > 0$, $p(\sigma,t)$ is a very steep narrow pulse concentrated near $t = 0$. The maximum value of $p(\sigma,t)$ is $(\pi\sigma^4 e^3/54)^{-1/2}$ and is attained at $t = t_{\max} = \sigma^2/6$, so that $p(\sigma,t)$ becomes the Dirac $\delta(t)$ as σ tends to 0. For larger σ, $p(\sigma,t)$ is a broad pulse, ultimately decaying to zero as t tends to infinity (see Fig. 1).

Dynamic Green's functions in transient wave propagation problems generally exhibit significant high-frequency oscillations and jumps, spikes, cusps, and various other sharp singularities. Such features are usually of vital interest in system identification. When $p(\sigma,t)$ is used as input into a linear system whose impulse response is $g(t)$, the resulting output response $h(t)$ is given by

$$\int_0^t p(\sigma,t-\tau)g(\tau)\,\mathrm{d}\tau = h(t), \qquad 0 \leq t < \infty \tag{3}$$

Such convolutions smooth out and distort the sharp features in $g(t)$, the more so the larger σ is chosen in Eq. (1). Use of small values of σ is desirable in order to minimize this blurring. On the other hand, in practice, the smallest value of σ that can be used will be dictated by the limitations of the actuator or pulsing device. It should be expected that $h(t)$ will bear little resemblance to $g(t)$, and that the integral equation (3) will need to be inverted in order to obtain $g(t)$.

This inversion is seriously affected by the presence of noise in the recorded data $h(t)$, as Eq. (3) is an example of an ill-posed problem. In any direct solution procedure, minute amounts of noise may be amplified to such an extent as to overwhelm the true solution. This may be anticipated by considering Eq. (3) in Laplace transform space. Write the recorded data $h(t)$ as

$$h(t) = h_e(t) + n(t) \tag{4}$$

where $h_e(t)$ is the exact response that would have been recorded in the absence of noise, while $n(t)$ is the deviation from the exact response due to noise and errors of all kinds, including roundoff errors in digitizing. Note that although $h(t)$ is known, each of $h_e(t)$ and $n(t)$ are unknown. Let $g_e(t)$ be the exact unique solution of Eq. (3) when $h_e(t)$ is used in place of $h(t)$. We assume there exist known positive constants ϵ and M such that

$$\int_0^\infty [g_e(t)]^2\,\mathrm{d}t \leq M^2, \qquad \int_0^\infty [n(t)]^2\,\mathrm{d}t \leq \epsilon^2, \tag{5}$$

with $\epsilon \ll M$, i.e.,

$$\omega = \epsilon/M \ll 1 \tag{6}$$

For any integrable function $f(t)$, let $F(s)$ be its Laplace transform:

$$F(s) = \int_0^\infty e^{-st}f(t)\,\mathrm{d}t, \qquad Re\, s > 0 \tag{7}$$

Taking Laplace transforms in Eq. (3) and using the convolution theorem together with the known transform of the inverse Gaussian, we get

$$e^{-\sigma\sqrt{s}}G(s) = H(s) = H_e(s) + N(s) \tag{8}$$

On the other hand,

$$e^{-\sigma\sqrt{s}}G_e(s) = H_e(s) \tag{9}$$

Applying Schwarz's inequality for integrals to $G_e(s)$ and to $N(s)$, and using Eq. (5), it easily follows that

$$|G_e(s)| \leq \frac{M}{\sqrt{2Re\, s}}, \qquad |N(s)| \leq \frac{\epsilon}{\sqrt{2Re\, s}}, \qquad Re\, s > 0 \tag{10}$$

Solving Eq. (8), we obtain

$$G(s) = G_e(s) + e^{\sigma\sqrt{s}}N(s) \tag{11}$$

Hence, from Eq. (10)

$$\frac{|G_e(s) - G(s)|}{|G_e(s)|} \geq \frac{\sqrt{2Re\, s}}{M}\,|e^{\sigma\sqrt{s}}||N(s)| \tag{12}$$

The positive exponential in Eq. (12) originates from inverting the inverse Gaussian kernel, and the inequality indicates that for large values of $|s|$, enormous relative errors in $G_e(s)$ will result from the presence of noise. Thus, legitimate high-frequency components in the true solution will be drowned out by spurious oscillations, originating from possibly very slight amounts of noise at these same frequencies in the recorded data $h(t)$. Larger values of σ lead to errors that become significant at relatively lower frequencies.

Such explosive error growth can be prevented by Tikhonov regularization. In the present case, this is equivalent to solving a modified problem defined as follows in the Laplace domain:

$$e^{-\sigma\sqrt{s}}G(s) = \frac{H(s)}{1 + \omega^2|e^{2\sigma\sqrt{s}}|} \tag{13}$$

with ω as in Eq. (6). Effectively, the recorded data are subjected to a probe-dependent low-pass filter prior to inverting the integral equation. The *regularization parameter* ω is defined in terms of the a priori information ϵ and M implied by Eq. (5), and represents the *noise to signal* ratio in the mean square (L^2) sense. In practice, the optimal value of ω is best found interactively starting from a plausible initial estimate. In contrast to the direct inversion case referred to in Eq. (12), the noise amplification factor remains bounded as a function of s in this regularized problem. We have

$$|G_e(s) - G(s)| \leq \frac{|N(s)||e^{\sigma\sqrt{s}}|}{1 + \omega^2|e^{2\sigma\sqrt{s}}|} + \frac{\omega^2|e^{2\sigma\sqrt{s}}|\,|G_e(s)|}{1 + \omega^2|e^{2\sigma\sqrt{s}}|} \tag{14}$$

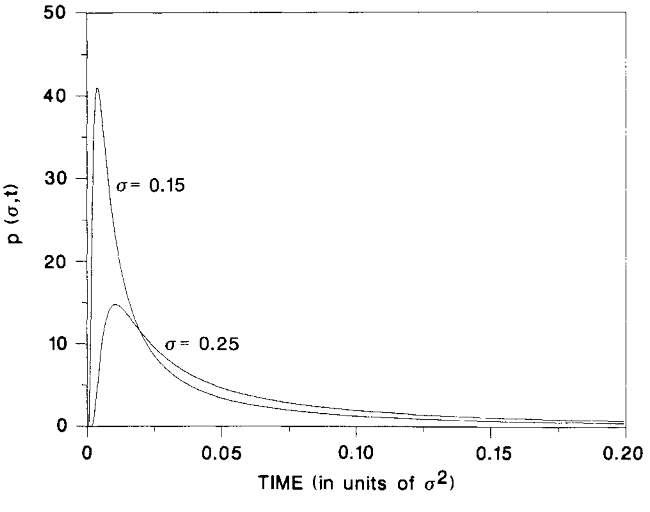

Fig. 1 Inverse Gaussian pulses.

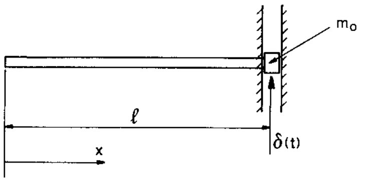

Fig. 2 Mechanical slider.

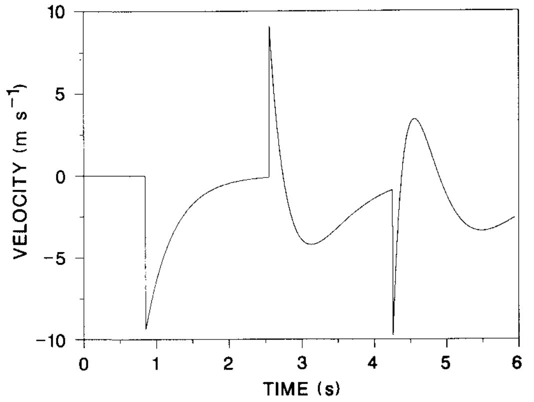

Fig. 3 Dynamic Green's function for mechanical slider.

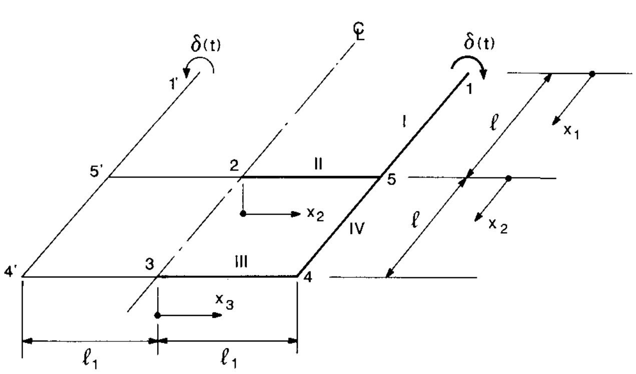

Fig. 4 Structural network.

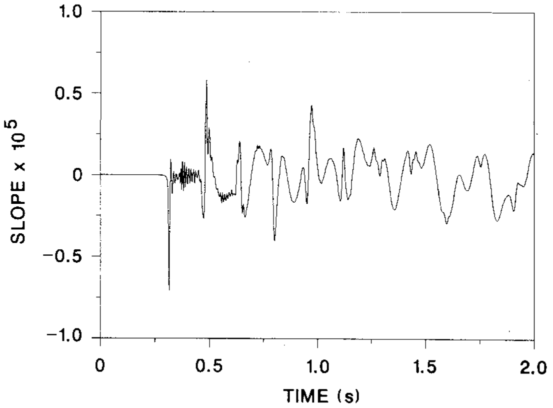

Fig. 5 Dynamic Green's function for structural network.

The factors multiplying $|N(s)|$ and $|G_e(s)|$ on the right of Eq. (14) are bounded by $(1/2\omega)$ and 1, respectively. Hence,

$$|G_e(s) - G(s)| \le \frac{|N(s)|}{2\omega} + |G_e(s)| \qquad (15)$$

This last inequality does not imply that the error in $G_e(s)$ is sufficiently small, only that it is bounded. In particular, the inequality does not guarantee that $G(s)$ obtained by solving Eq. (13) is a better approximation to $G_e(s)$ than is the trivial solution $G(s) \equiv 0$, and the possibility of spurious noise artifacts producing an erroneous solution is not entirely ruled out in the above Tikhonov regularization. Nevertheless, in practice, surprisingly accurate solutions are often found by proper choice of ω. Thus, there is a need for supplementary information that can help ascertain whether or not the reconstructed Green's function approximates the true system's impulse response. In this connection, the inverse Gaussian pulse has a useful mathematical property that can be used to monitor the deconvolution process.

For any positive integer m, an inverse Gaussian with parameter σ may be viewed as the m-fold convolution of m distinct inverse Gaussians, each with parameter (σ/m):

$$p(\sigma,t) = \{p[(\sigma/m),t]\}^{*m} \qquad (16)$$

One may then consider the blurred data $h(t)$ in Eq. (3) to have been obtained from $g(t)$ as a result of m successive slight blurs, each with a narrow pulse $p[(\sigma/m),t]$. This decomposition property is one that the inverse Gaussian shares with a rich class of probes, the so-called *infinitely divisible* probes.[7] Choosing $m = 20$ say, one may solve the regularized problem by removing the m convolution factors one at a time, and obtain the reconstructed impulse response as the end result of a sequence of m partial deconvolutions. Each narrow pulse removal undoes a slight amount of the total blur caused by $p(\sigma,t)$, while contributing a small amount to the total finite amount of noise amplification in the regularized problem. Most importantly, one can bound the error[7] in the partial deconvolutions in terms of the mean square noise level ϵ in Eq. (5), and be assured to convergence as ϵ tends to zero, whereas this is not possible in Eq. (15). As more factors are removed, the sharp features in the desired Green's function begin to appear. The solution becomes *sharper* and *noisier* until, eventually, total deconvolution is achieved when all m convolution factors have been removed. A graphical display of the sequence of partial deconvolutions is helpful to the analyst in distinguishing systematic trends from noise artifacts. For example, a sharp spike or cusp in the total deconvolution can be confirmed, if its genesis can be traced back to an early (and rigorous) partial deconvolution; [see, e.g. Figs. 6(a) and 13 in Ref. 7 and Fig. 9 below]. We refer to this process as deconvolution in *slow motion.*

Although the pulse probing technique is a time domain technique, the numerical computations are carried out in the complex frequency domain via the Fast Fourier Transform (FFT). The algorithm[7] uses as input the digitized time domain waveforms for the probe pulse and the recorded data, given at $2N$ equispaced points on the finite time interval $[0,2T]$, with N and T sufficiently large. One first uses the algorithm to proceed directly to the regularized total deconvolution. Here, experimentation using interactive graphics is highly recommended in locating the optimal value of ω. Values of ω that do not lead to noise in the total deconvolution are probably too large; very likely, legitimate high-frequency behavior in the solution has been smoothed out along with the noise. A very noisy total deconvolution indicates that ω is probably too small. A range of ω values is quickly found for which little change in the total deconvolution is visible. At this stage, one should verify and analyze the genesis and development of sharp features by performing the deconvolution in slow motion. The stability of this evolution to small changes in ω may also be studied, and further adjustments made.

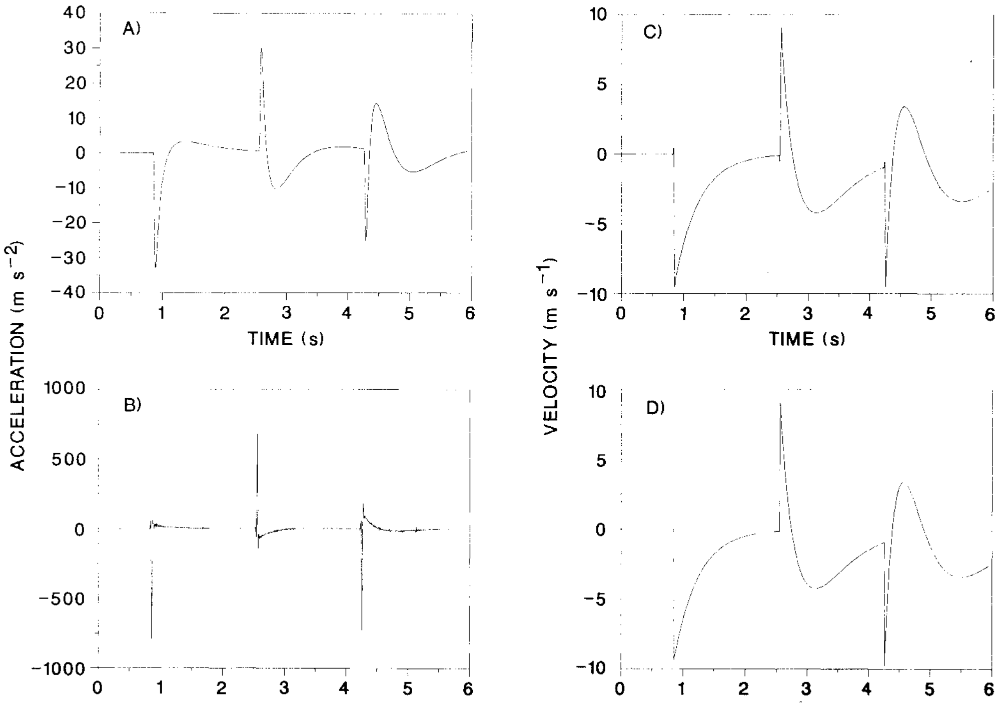

Fig. 6 Reconstruction of slider Green's function for tip velocity (1% noise; $\omega = 10^{-4}$).

Dynamic Green's Functions: Examples

To illustrate the application of the deconvolution technique described above, we consider two structural examples. The first example is nondispersive and exhibits jump discontinuities. The second example is dispersive, and high-frequency oscillations constitute an important part of the impulse response. Knowledge of the exact Green's functions in these examples provides the basis for evaluating the accuracy of the deconvolution technique.

Mechanical Slider

This structure models a vertically translating robot arm (Fig. 2) and consists of a horizontal bar, free at one end, and rigidly connected at the opposite end to a perfectly rigid hub that may slide in the vertical direction. The dynamics of this member and of similar types of members are of interest in the study of flexible robot arms with noncollocated controls in which the actuator is located at the hub, and the effector is located at the free end.[2,8] As in Refs. 2 and 8, we use the values $\rho A = 0.425$ kg/m for the mass per unit length of the bar, and $l = 1.1$ m for the length of the bar. We assume further that the shear stiffness is given by $GA_s = 0.711(1 + i\eta)$, where the hysteretic damping $\eta = 0.01$. (These parameters were developed in Ref. 2 in an attempt to obtain an equivalent beam whose response would match the measured response of the flexible robot arm studied in Ref. 8). Finally, we use $m_0 = 0.2125$ kg as the mass of the hub, and assume the bending stiffness of the bar to be sufficiently large that bending deflections are negligible compared to deflections due to shearing strain. As shown in the Appendix, owing to this last assumption the structure is nondispersive, and its dynamic Green's function can be obtained in closed form.

Figure 3 shows the velocity at $x = 0$ due to the unit impulsive force $\delta(t)$ shown in Fig. 2, for $0<t<7l/a$ where $a^2 = GA_s/\rho A$. After a lag l/a corresponding to the transit time of the impulse, the velocity at $x = 0$ experiences a jump discontinuity; further jumps follow at intervals of $2l/a$, corresponding to round-trip transits of the disturbance from the free end to the hub.

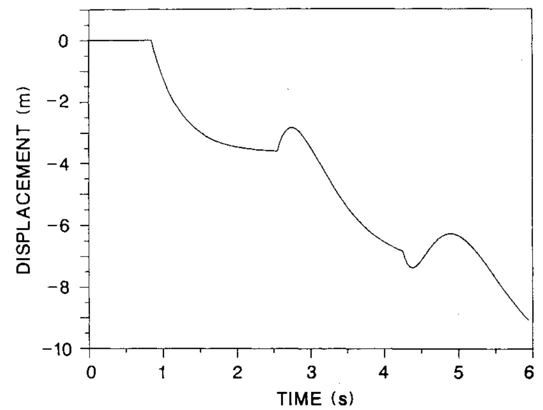

Fig. 7 Slider Green's function for tip displacement (1% noise; $\omega = 10^{-4}$).

Structural Network

The second example is a network (Fig. 4) consisting of four identical torsional members (1 − 5, 5 − 4, 1′ − 5′, and 5′ − 4′) and two identical Timoshenko beams (4 − 4′ and 5 − 5′). The members are rigidly connected at joints 4, 4′, 5, 5′. The network is symmetrical about the midpoints of beams 5 − 5′ and 4 − 4′, denoted by 2 and 3, respectively. Comparable networks have been used as examples of hypothetical large space structures in Refs. 2 and 3. We assume the following member properties.[2,3]

Timoshenko beams: mass per unit length, $\rho A = 2.39$ kg/m; mass moment of inertia about the neutral axis per unit length, $\rho I = 11.8$ kgm; bending stiffness, $EI = 1.77 \times 10^8(1 + i\eta)$ Nm^2; shear stiffness, $GA_s = 2.94 \times 10^6(1 + i\eta)$; $\eta = 0.01$; length, $l_1 = 97.5$ m.

Torsional members: mass moment of inertia about axis of member, $\rho_1 J = 23.6$ kgm; torsional stiffness, $G_1 J = 3.67 \times 10^7(i + i\eta)$ Nm^2; $\eta = 0.01$; length, $l = 97.5$ m.

The Green's function being sought is the slope of member III at joint 4 due to the unit impulsive moments shown in Fig.

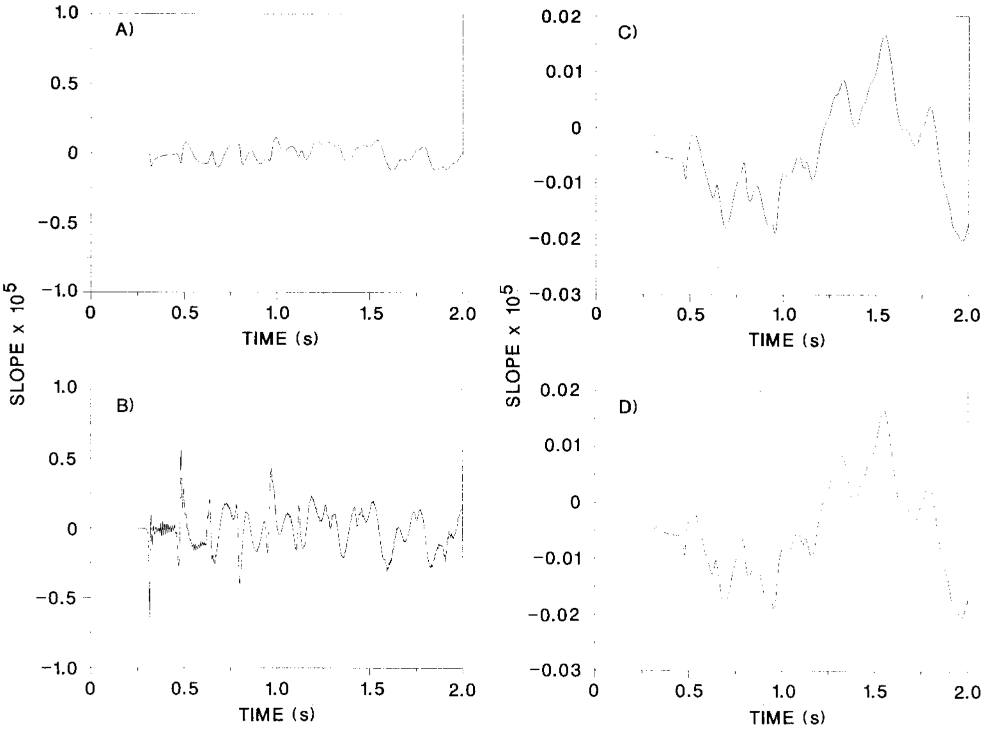

Fig. 8 Reconstruction of network Green's function (1% noise; $\omega = 1.75 \times 10^{-3}$).

4, and its calculation is described in the Appendix. It is shown in Fig. 5 for $0<t<2s$. Noteworthy features include a lag corresponding to the transit time of the impulsive torsion wave, a sharp spike indicating the arrival of that wave, and high-frequency oscillations due to the subsequent arrivals of dispersive waves from the Timoshenko beams.

Numerical Reconstruction Experiments

Our aim is to demonstrate the possibility of accurate reconstruction of structural Green's functions, from measured responses to actuator-controlled inverse Gaussian sources. As indicated by Eqs. (3) and (4), we may use the exact Green's functions shown in Figs. 3 and 5 to create synthetic noisy data $h(t)$ simulating such responses.

Consider first the mechanical slider problem, where we imagine the response at the free end $x = 0$ to be measured by an accelerometer. The exact velocity in Fig. 3 was numerically differentiated and then convolved with the pulse $p(\sigma,t)$ given in Eq. (1). A value of $\sigma = 0.5\, s^{1/2}$ was selected, leading to a pulse with a rise time of $t_{\max} = \sigma^2/6 = 41.67$ ms. The discontinuities in the velocity at $t = l/a$, $3l/a$, and $5l/a$ result in δ-function behavior at these points in the exact acceleration curve. However, the convolution process smooths out these spikes considerably; the blurred acceleration, shown in Fig. 6a, was evaluated at 1000 equispaced points on the time interval $(0, 7l/a)\, s$ using adaptive quadrature routines. Next, each of the 1000 convolved data values y was perturbed by adding to it a random number drawn from a uniform distribution in the range $\pm 0.01y$. We refer to this process as "adding 1% noise." These data, together with the digitized inverse Gaussian, constitute the input data for the deconvolution procedure. The reconstruction of the acceleration with the regularization parameter $\omega = 1.0 \times 10^{-4}$ is shown in Fig. 6b. Considerable sharpening of the peaks has evidently occurred, with the amplitudes in Fig. 6b being from 20-30 times greater than the corresponding values in Fig. 6a. Some "ringing" and noise artifacts are also clearly apparent. However, due to the scaling demanded by the spikes, the structure of the acceleration curve between the peaks is not visible in Fig. 6b.

The reconstructed velocity shown in Fig. 6c was obtained by cumulative summation of the discrete data in Fig. 6b, and is in very good agreement with the exact velocity, shown in Fig. 6d. Such integration is an averaging process that is helpful in reducing noise effects and other pointwise errors. Indeed, a further integration of the reconstructed velocity results in a reconstructed displacement curve that is visually indistinguishable from the exact displacement curve, as shown in Fig. 7 where the two curves are superimposed. Higher accuracy can be achieved in Figs. 6b and 6c using narrower probing pulses. The robustness of the deconvolution procedure in the presence of discontinuities is surprisingly good, however.

In the case of the structural network, the time scale for dynamic effects is finer than that for the slider. Accordingly, a value of $\sigma = 0.2\, s^{1/2}$ was selected for the probing pulse, corresponding to a rise time of 6.67 ms. The resulting blurred response, shown in Fig. 8a, bears little resemblance to the δ-response of Fig. 5. As in the previous case, 1000 equispaced points were used on the interval $0<t<2\, s$, and 1% noise was added to the blurred signal. The regularized reconstruction of the δ-response, using $\omega = 1.75 \times 10^{-3}$, is shown in Fig. 8b. Much of the detailed structure in this complex Green's function has been reproduced. However, a close inspection of Fig. 8b reveals the following discrepancies: the sharp peaks in the early part of the signal have been microscopically rounded; the dispersive behavior immediately following the arrival of the torsion wave has not been exactly reproduced; and extraneous high-frequency oscillations, originating in noise, linger near the end of the interval. These discrepancies are of little consequence when the reconstructed Green's function is used as a tool in predicting the response to a given smooth forcing function $f(t)$, as the convolution process will average out such small pointwise errors. As an example, the reconstructed *step response* (Fig. 8c), obtained by cumulative summation of the data in Fig. 8b, is virtually indistinguishable from the exact step response (Fig. 8d).

We now illustrate the process of going from Fig. 8a to Fig. 8b in slow motion. In Fig. 9, two different views of this evolution are displayed. In the top drawing, the decomposition property of the inverse Gaussian, Eq. (16), was used to pro-

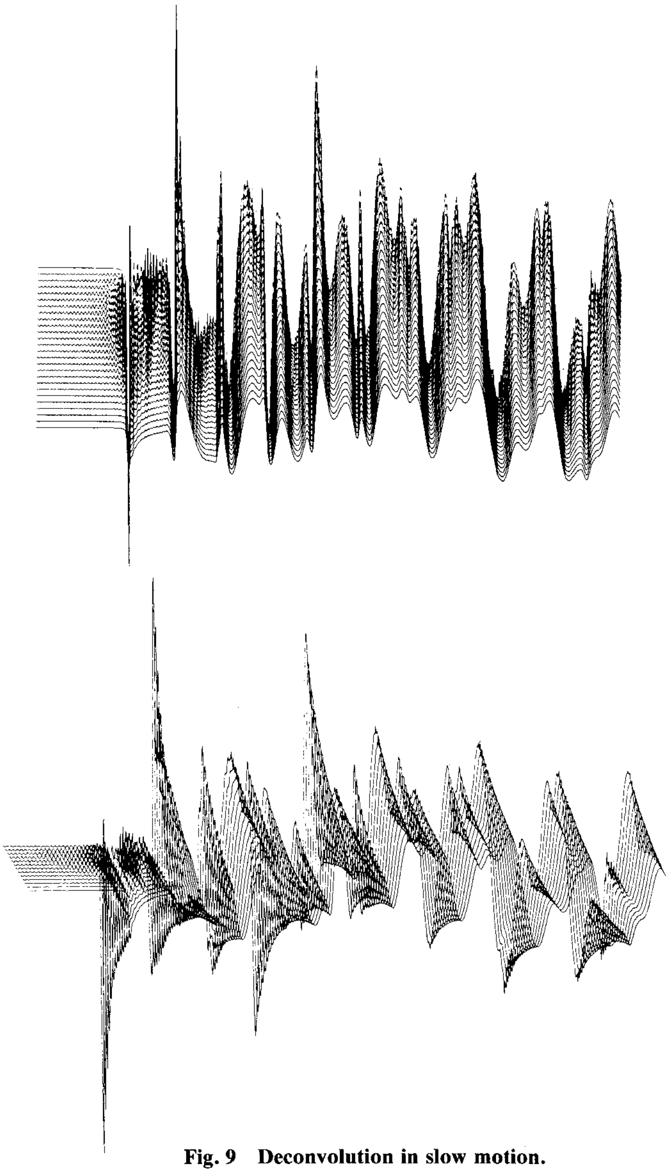

Fig. 9 Deconvolution in slow motion.

ceed from the blurred signal $b_1(t)$, (first trace in foreground), to the unblurred signal $b_{26}(t)$, (last trace in background), in 25 discrete steps. Each trace $b_k(t)$ is related to its predecessor according to the formula,

$$\int_0^t p\left(\frac{\sigma}{25}, t-\tau\right) b_k(\tau)\,\mathrm{d}\tau = b_{k-1}(t), \quad k = 2,3,\ldots,26 \qquad (17)$$

In the bottom drawing, a different viewing angle was selected, and 12 discrete steps were used. The top drawing is a view from above of the bottom drawing. Such diagrams make it possible to study the development of specific features in the solution. And, given the nature of the error bound in Eq. (15), they may prove useful in practice in validating unexpected behavior in a structural Green's function.

Conclusion

A mathematical and computational capability exists that would enable reliable experimental determination of dynamic Green's functions for structural systems. The method is based on propagating specific types of pulses leading to a tractable deconvolution problem in the presence of noise. Computational experiments can assist in the design of instrumentation by predicting the quality of information that can be retrieved at given levels of data noise, and with varying rise times for the input probe.

Appendix: Derivation of Exact Green's Functions

Mechanical Slider

The equation of motion and the constitutive equation for the slider (Fig. 2) are, respectively,

$$\frac{\partial V}{\partial x} = \rho A \frac{\partial^2 w}{\partial t^2}, \qquad \frac{\partial w}{\partial x} = \frac{V}{GA_s} \qquad (A1)$$

so that

$$\frac{\partial^2 w}{\partial t^2} = a^2 \frac{\partial^2 w}{\partial x^2}, \qquad a^2 = \frac{GA_s}{\rho A} \qquad (A2)$$

where V is the shear force, x is the horizontal coordinate, ρA is the mass per unit length, w is the deflection, t is the time, and GA_s is the shear stiffness. The boundary conditions are

$$V|_{x=0} = 0, \qquad \left(\text{or } \frac{\partial w}{\partial x}|_{x=0} = 0\right) \qquad (A3)$$

$$m_0 \frac{\partial^2 w}{\partial t^2}|_{x=l} = -\delta(t) - V|_{x=l} \qquad (A4)$$

where m_0 is the mass of the hub.

A classical solution to an entirely analogous problem[9] was applied and extended to the range $2l/a < t < 6l/a$ ($x = l$) as follows. First note that Eq. (A4) is a condensed representation of the boundary condition

$$\frac{m_0}{\rho A} \frac{\partial^2 w}{\partial t^2}|_{x=l} = -a^2 \frac{\partial w}{\partial x}|_{x=l} \qquad (A5)$$

and the initial conditions

$$w|_{t=0} = 0, \qquad 0<x<l, \qquad \lim_{t=+0} \frac{\partial w}{\partial t}|_{x=l} = -\frac{1}{m_0} \qquad (A6)$$

and that the first of Eqs. (A6) implies

$$\frac{\partial w}{\partial x}|_{t=0} = 0 \quad \text{and} \quad \frac{\partial w}{\partial t}|_{t=0} = 0, \qquad 0<x<l \qquad (A7)$$

Respectively, $t = 0$ and $t = +0$ are the times just before and after the action of the impulsive load $\delta(t)$

The general solution of Eq. (A2) is

$$w = f(at - x) + F(at + x) \qquad (A8)$$

From Eq. (A3) and the first of Eqs. (A6) it follows that

$$w = f(at - x) + f(at + x) \qquad (A9)$$

Using Eq. (A7) and the first of Eqs. (A6) (for $x = 0$) we get

$$f(\zeta) = 0, \qquad -l<\zeta<l \qquad (A10)$$

The *continuing equation* is then derived from Eq. (A5):

$$f''(\zeta) + \frac{\rho A}{m_0} f'(\zeta) = -f''(\zeta - 2l) + \frac{\rho A}{m_0} f'(\zeta - 2l) \qquad (A11)$$

The integral of Eq. (A11) is of the form

$$f'(\zeta) = Ce^{-\rho A\zeta/m_0} + e^{-\rho A\zeta/m_0} \int_0^\zeta e^{\rho A\zeta/m_0} \times \left(-f''(\zeta - 2l) + \frac{\rho A}{m_0} f'(\zeta - 2l)\right) \mathrm{d}\zeta \qquad (A12)$$

For $l<\zeta<3l$, the integrand in Eq. (A12) vanishes [see Eq. (A10)], and using the second of Eqs. (A6) together with the condition that there be no sudden change in the displacement at $x = l$, one obtains

$$f'(\zeta) = -\frac{1}{am_0}e^{-\rho A(\zeta - l)/m_0}, \qquad l<\zeta<3l \tag{A13}$$

$$f(\zeta) = -\frac{1}{a\rho A}\left(1 - e^{-\rho A(\zeta - l)/m_0}\right), \qquad l<\zeta<3l \tag{A14}$$

For $3l<\zeta<5l$, using Eqs. (A12), (A13), and the conditions that 1) the velocity be continuous at $x = l$, $t = 2l/a$, and 2) there be no sudden change in the displacement at $x = l$, we get

$$\begin{aligned} f'(\zeta) = &-\frac{1}{am_0}e^{-\rho A(\zeta - l)/m_0} \\ &+\frac{1}{am_0}\left(1-\frac{2\rho A(\zeta-3l)}{m_0}\right)e^{-\rho A(\zeta-3l)/m_0} \\ &3l<\zeta<5l \end{aligned} \tag{A15}$$

$$\begin{aligned} f(\zeta) = &\frac{1}{a\rho A}\left[-2+e^{-\rho A(\zeta-l)/m_0}\right. \\ &\left.+\left(1+\frac{2\rho A(\zeta-3l)}{m_0}\right)\times e^{-\rho A(\zeta-3l)/m_0}\right] \\ &3l<\zeta<5l \end{aligned} \tag{A16}$$

For $5l<\zeta<7l$, we obtain using the same approach:

$$\begin{aligned} f'(\zeta) = &-\frac{1}{am_0}e^{-\rho A(\zeta-l)/m_0}+\frac{1}{am_0}\left(1-\frac{2\rho A}{m_0}(\zeta-3l)\right) \\ &\times e^{-\rho A(\zeta-3l)m_0}-\frac{1}{am_0}\left(1-\frac{4\rho A}{m_0}(\zeta-5l)\right. \\ &\left.+2\left(\frac{\rho A}{m_0}\right)^2(\zeta-5l)^2\right)\times e^{-\rho A(\zeta-5l)/m_0} \\ &5l<\zeta<7l \end{aligned} \tag{A17}$$

$$\begin{aligned} f(\zeta) = &\frac{1}{a\rho A}\left(-3+e^{-\rho A(\zeta-l)m_0}\right)+\left(\frac{1}{a\rho A}+\frac{2}{am_0}(\zeta-3l)\right) \\ &\times e^{-\rho A(\zeta-3l)/m_0}+\left(\frac{1}{a\rho A}+\frac{2\rho A}{am_0^2}(\zeta-5l)^2\right) \\ &\times e^{-\rho A(\zeta-3l)/m_0}, \qquad 5l<\zeta<7l \end{aligned} \tag{A18}$$

Note that using Eqs. (A1–A3), Eq. (A4) can be written in the form

$$\int_0^l \rho A\frac{\partial^2 w}{\partial t^2}\,\mathrm{d}x + m_0\frac{\partial^2 w(l,t)}{\partial t^2} = -\delta(t) \tag{A19}$$

From Eq. (A19) we get, on integrating twice with respect to t,

$$w_G = -\frac{t}{\rho A l + m_0} \tag{A20}$$

where w_G is the ordinate of the instantaneous center of mass of the moving system, i.e.,

$$w_G = \frac{\int_0^l \rho A w(x,t)\,\mathrm{d}x + m_0 w(l,t)}{\rho A l + m_0} \tag{A21}$$

On using Eqs. (A10), (A14), (A16), and (A18), it can be verified that Eq. (A20) is satisfied by Eq. (A9).

Structural Network

In the following derivations, we take advantage of symmetry and consider only the right half of the network (represented by heavy lines in Fig. 4 and consisting of the members denoted by 1, II, III, and IV).

The equation of motion for a torsional member and the constitutive relation under the assumption of linearly elastic behavior are, respectively,

$$\frac{\partial T}{\partial x} = \rho_1 J\frac{\partial^2\theta}{\partial t^2}, \qquad \frac{\partial\theta}{\partial x} = \frac{T}{JG_1} \tag{A22}$$

where T is the torque, $\rho_1 J$ is the mass moment of inertia about the axis of the number, θ is the angular deformation, and JG_1 is the torsional stiffness. We now Fourier transform the time dependence in Eqs. (A22) and use ξ to denote the circular frequency. For a member of length l, the general solution of Eqs. (A22) is then

$$\bar\theta(x) = \bar\theta(0)\cos\left(\frac{\lambda x}{l}\right) + \bar T(0)\frac{l}{\lambda JG_1}\sin\left(\frac{\lambda x}{l}\right) \tag{A23}$$

$$\lambda = \left(\frac{\rho_1 J}{JG_1}\right)^{1/2} l\xi \tag{A24}$$

where $\bar\theta$, $\bar T$ denote the Fourier transforms of θ and T. A similar relation for $\bar T(x)$ is obtained for the second of Eqs. (A22). We denote the rotation of member I at $x_1 = 0$ and $x_1 = l$, by θ_{10} and θ_{1l}, respectively; the corresponding torques by T_{10} and T_{1l}; and the corresponding quantities for member IV by θ_{40}, θ_{4l}, T_{40}, T_{4l}.

Timoshenko beams are *dispersive* members for which the equations of motion are[10]

$$\frac{\partial V}{\partial x} = \rho A\frac{\partial^2 w}{\partial t^2}, \qquad \frac{\partial M}{\partial x} - V = \rho I\frac{\partial^2\psi}{\partial t^2} \tag{A25}$$

with the constitutive relations

$$M = EI\frac{\partial\psi}{\partial x}, \qquad V = GA_s\left(\frac{\partial w}{\partial x} + \psi\right) \tag{A26}$$

where M is the bending moment, ρI is the mass moment of inertia about the neutral axis per unit length, EI is the bending stiffness, ψ is the angular deformation due to bending, and the other notations are the same as in Eq. (A1).

The "state variable" vector y is defined by

$$\{y\} = \{-w, \psi, M, V\}^T \tag{A27}$$

The Fourier transforms of Eqs. (A25) and (A26) yield a fourth-order system of equations whose eigenvalues are denoted by $\pm\lambda_1$ and $\pm\lambda_2$. The general solution for the Fourier transform of V is[11]

$$\begin{aligned} \bar V = &A_1\cosh\left(\frac{\lambda_1 x}{l}\right) + A_2\sinh\left(\frac{\lambda_1 x}{l}\right) \\ &+ A_3\cos\left(\frac{\lambda_2 x}{l}\right) + A_4\sin\left(\frac{\lambda_2 x}{l}\right) \end{aligned} \tag{A28}$$

General solutions for $\bar w$, $\bar\psi$, and $\bar M$ follow immediately from Eq. (A28) and the Fourier transforms of Eqs. (A25) and (A26). The Fourier transforms of the state variables $\{\bar y\}$ for beams II and III are denoted by $\{\bar y_2\}$ and $\{\bar y_3\}$, respectively.

The boundary conditions for the network are

Joint 1:

$$\bar{T}_{10} = 1 \tag{A29}$$

Joint 2:

$$\bar{V}_2|_{x_2=0} = 0, \qquad \frac{\mathrm{d}\bar{w}_2}{\mathrm{d}x_2}|_{x_2=0} = 0 \tag{A30}$$

Joint 3:

$$\bar{V}_3|_{x_3=0} = 0, \qquad \frac{\mathrm{d}\bar{w}_3}{\mathrm{d}x_3}|_{x_3=0} = 0 \tag{A31}$$

Joint 4:

$$\bar{V}_3|_{x_3=l_1} = 0, \quad \bar{M}_3|_{x_3=l_1} - \bar{T}_{4l} = 0, \quad \frac{\mathrm{d}\bar{w}_3}{\mathrm{d}x_3}|_{x_3=l_1} = \bar{\theta}_{4l} \tag{A32}$$

Joint 5:

$$\bar{V}_2|_{x_2=l_1} = 0, \qquad \bar{M}_2|_{x_2=l_1} - \bar{T}_{1l} - \bar{T}_{40} = 0, \qquad \bar{\theta}_{1l} = \bar{\theta}_{40},$$

$$\frac{\mathrm{d}\bar{w}_2}{\mathrm{d}x_2}|_{x_2=l_1} = \bar{\theta}_{1l} \tag{A33}$$

From Eqs. (A29–A33) it follows that the slope of member III at joint 4 due to the unit impulsive moments shown in Fig. 3 is

$$\frac{\mathrm{d}\bar{w}_3}{\mathrm{d}x_3}|_{x_3=l_1} = \left[\cos^2\lambda + \frac{c_1(\xi)l\sin\lambda}{\lambda JG_1}\right]\left\{\frac{c_2^2(\xi)\cos\lambda - c_3(\xi)}{c_1(\xi)[c_2(\xi)-1]}\right\}$$

$$+ [1 - c_2(\xi)]\left(\frac{l\sin\lambda\cos\lambda}{\lambda JG_1}\right) \tag{A34}$$

$$c_1(\xi) = -\left[c_4(\xi)\cos\lambda + JG_1\frac{\lambda\sin\lambda}{l}\right] \tag{A35}$$

$$c_2(\xi) = -1 + c_4(\xi)\frac{l\tan\lambda}{\lambda JG_1} \tag{A36}$$

$$c_3(\xi) = c_4(\xi)\frac{l\sin\lambda}{\lambda JG_1} + \frac{\sin^2\lambda}{\cos\lambda} \tag{A37}$$

$$c_4(\xi) = -\frac{EI}{\lambda_1^2 + \lambda_2^2}\left[(\beta + \lambda_1^2)\frac{\lambda_1}{l_1\tanh\lambda_1} - (\beta - \lambda_2^2)\frac{\lambda_2}{l_1\tan\lambda_2}\right] \tag{A38}$$

where

$$\beta = \frac{\rho A\xi^2 l^2}{GA_s} \tag{A39}$$

It can be verified that for ξ vanishingly small, $\bar{\theta}_{4l}$ approaches the static solution

$$\theta_{4l}^{\mathrm{st}} = -\frac{l_1}{EI}\left(2 + \frac{lEI}{l_1G_1J}\right)^{-1} \tag{A40}$$

The Green's function is obtained by taking the inverse Fourier transform of Eq. (A34).

Acknowledgments

The research was sponsored by the Directorate of Aerospace Sciences, Air Force Office of Scientific Research. Dr. Anthony K. Amos served as the project monitor.

References

[1] Butkovskiy, A. G., *Green's Functions and Transfer Function Handbook,* Wiley, New York, 1982.

[2] von Flotow, A. H., "Disturbance Propagation in Structural Networks; Control of Large Space Structures," Ph.D. Dissertation, Dept. of Aeronautics and Astronautics, Stanford Univ., Stanford, CA, June 1984.

[3] von Flotow, A. H., "Disturbance Propagation in Structural Networks," *Journal of Sound and Vibration,* Vol. 106, No. 3, May 1986, pp. 433–450.

[4] Ibrahim, S. R., "Modal Identification Techniques; Assessment and Comparison," *Sound and Vibration,* Vol. 19, Aug. 1985, pp. 10–15.

[5] Stroud, R. C., "Excitation, Measurement, and Analysis Methods for Modal Testing," *Sound and Vibration,* Vol. 21, Aug. 1987, pp. 12–27.

[6] Halvorsen, W. G. and Brown, D. L., "Impulse Technique for Structural Frequency Response Testing,' *Sound and Vibration,* Vol. 11, Nov. 1977, pp. 8–21.

[7] Carasso, A. S., "Infinitely Divisible Pulses, Continuous Deconvolution, and the Characterization of Linear Time Invariant Systems," *SIAM Journal on Applied Mathematics,* Vol. 47, Aug. 1987, pp. 892–997.

[8] Cannon, R. H., Jr., and Schmitz, E., "Initial Experiments on the End-Point Control of a Flexible One-Link Robot," *The International Journal of Robotics Research,* Vol. 3, Fall 1984, pp. 62–75.

[9] Love, A. E. H., *A Treatise on the Mathematical Theory of Elasticity,* 4th ed., Dover, New York, 1944, p. 431.

[10] Hurty, W. C. and Rubinstein, M. F., *Dynamics of Structures,* Prentice-Hall, Englewood Cliffs, NJ, 1964, p. 88.

[11] Pestel, E. C. and Leckie, F. A., *Matrix Methods in Elastomechanics,* McGraw-Hill, New York, 1963 p. 133.